PCCP

PAPER

View Article Online
View Journal | View Issue

Cite this: *Phys. Chem. Chem. Phys.*, 2018, **20**, 28759

Edge morphology induced rectifier diode effect in C_3N nanoribbon†

Jing-Jing He, [ab] Yan-Dong Guo, *[ab] Xiao-Hong Yan*[abcd] and Hong-Li Zeng[be]

Received 15th August 2018,
Accepted 23rd October 2018

DOI: 10.1039/c8cp05209c

rsc.li/pccp

The two-dimensional material C_3N has a honeycomb structure similar to graphene, but its heterogeneity of carbon and nitrogen elements makes it multifunctional. By performing a first-principles study, we find that edge morphology induces interesting electronic transport properties in step-like heterojunction devices composed of width-variable zigzag C_3N nanoribbons. As long as the right part has an edge of all-carbon morphology, negative differential resistance and rectification effects will occur. If both edges are not of all-carbon morphology due to the presence of N atoms, a forward-conducting and reverse-blocking rectifier diode behavior will appear. These phenomena originate from the peculiar electronic structure of the zigzag C_3N nanoribbons. The number of energy bands crossing the Fermi level gradually decreases from 2 to 0 as the number of all-carbon edges decreases, realizing a transition from metal to semiconductor. The band gap determines the cut-off region at low bias and the presence of an interface barrier causes the cut-off state to continue under high reverse bias. Diverse edge morphologies, simple cutting methods and rich electronic transport properties make C_3N materials competitive in nanodevice applications.

Introduction

Since the discovery of graphene, two-dimensional (2D) materials have become a research hotspot.[1–4] A new 2D layered material C_3N, similar to graphene, also has a honeycomb lattice structure, however, unlike the all-carbon composition of graphene, both carbon and nitrogen heteroatoms are evenly distributed, with three sp^2 carbons sharing a tertiary nitrogen.[5–9] It is due to the presence of the nitrogen atoms that C_3N opens a band gap, which is different from the metallicity of graphene. Recently, the 2D material C_3N has been successfully prepared by Mahmood's and Yang's groups using different methods. Mahmood *et al.*[6] used direct pyrolysis of hexaaminobenzene trihydrochloride (HAB) single crystals in the solid state, while Yang *et al.*[5] conducted a controllable large-scale synthesis by polymerization of 2,3-diaminophenazine (DAP). The as-prepared C_3N shows an indirect band gap of 0.39 eV which will increase with decreasing quantum dot size to in excess of 2.74 eV.[5] A back-gate field-effect transistor made of monolayer C_3N exhibits an on–off current ratio up to 5.5×10^{10}.[5] Theoretically, the first-principles study of Wang's research group[10] demonstrates that monolayer C_3N has high stability and ultra-high mechanical strength, and its Young's modulus of 1090.0 GPa is higher than the 1057.7 GPa of graphene. In addition, monolayer C_3N is an indirect bandgap semiconductor (1.09 eV) with a strong polar covalent bond, while multilayered C_3N with an AD stack exhibits metallicity.[10]

A variety of interesting electronic transport properties have been found in nanodevices based on 2D materials, such as negative differential resistance (NDR),[11–14] rectification,[15–17] spin filtering,[18–21] switching[22–24] and field-effect transistors.[25–27] Among them, rectification, which has been widely reported in molecular nanodevices, has attracted considerable attention and also been extensively studied in graphene heterojunctions.[28–35] Li *et al.*[36] found pronounced rectification behavior in armchair-zigzag graphene nanoribbon heterojunctions, and this strongly depends on the width of the junction. The revealed microscopic mechanism originates from the inherent asymmetry of the aGNR–zGNR heterojunction which can induce asymmetrical motion of resonance and interference. Cao *et al.*[37] reported that both bare-dihydrogenated and monohydrogenated–dihydrogenated ZGNR heterojunctions exhibit rectification characteristics which are caused by the different mirror operation symmetry of the bands near the Fermi level. A. R. Cadore *et al.*[38] studied

[a] College of Electronic and Optical Engineering, Nanjing University of Posts and Telecommunications, Nanjing 210023, China. E-mail: yandongguo@njupt.edu.cn, yanxh@njupt.edu.cn
[b] Key Laboratory of Radio Frequency and Micro Nano Electronics of Jiangsu Province, Nanjing 210023, China
[c] College of Science, Nanjing University of Aeronautics and Astronautics, Nanjing 210016, China
[d] School of Material Science and Engineering, Jiangsu University, Zhenjiang, 212013, China
[e] College of Natural Science, Nanjing University of Posts and Telecommunications, Nanjing 210046, China

† Electronic supplementary information (ESI) available. See DOI: 10.1039/c8cp05209c

the graphene–metal heterojunction and found an asymmetrical resistance in electronic transport for electrons and holes due to an electrostatic interaction, and this can be tuned in a reversible manner by exposing graphene devices to H_2. In addition, rectification has also been investigated in graphene-like heterojuctions, *e.g.*, partially edge-hydrogenated MoS_2 nanoribbon heterostructures[39] and bare-monohydrogenated phosphorene heterojunctions.[35] Experimentally, Young and Kim[40] prepared extremely narrow graphene heterojunctions and found magnetic-field-dependent oscillatory conductance as a result of quantum interference and Klein tunnelling effects.[36]

Recently, Ma *et al.*[41] fabricated a step-like armchair graphene nanoribbon heterojunction using a surface-assisted self-assembly process to achieve seamless staircase electrical contact. An *et al.*[42] performed first-principles calculations on step-like graphene nanoribbons and studied the regulation of the width of the step on the electronic transport properties. Motivated by these theoretical and experimental studies, we pay our attention to the newly prepared 2D material C_3N. It is worth noting that, unlike pure-carbon graphene, changes in the width of the C_3NNR also cause changes in the edge morphology (all-carbon or C–N mixed morphology). So, for a step-like C_3N heterojunction, in addition to the step, the edge morphology is also an essential factor to be considered. The impact of the dual regulation mechanism on the electronic transport property of the step-like heterojunction of the new material C_3N deserves further study. In this paper, we construct a step-like heterojunction (HJ) device composed of width-variable zigzag C_3N nanoribbons (ZC_3NNRs), *i.e.*, a fixed left part and a changing right part with increasing width. The calculations conclude that the change in edge morphology can effectively regulate the electronic properties of the ZC_3NNRs, thereby changing the nature of the heterojunction (switching between metal–metal contact and metal–semiconductor contact). NDR and rectification effects will occur in HJs if the right part has an edge of all-carbon morphology, and the greater the step, the more obvious the rectification phenomenon. Interestingly, forward-conducting and reverse-blocking rectifier diode behavior appears in HJs with N atoms on both edges of the right part.

Methodology

The calculations are performed using the Atomistix Toolkit (ATK) package, which is based on a combination of density functional theory (DFT) and the non-equilibrium Green's function (NEGF) technique.[43] The Perdew–Burke–Ernzerhof formulation of the generalized gradient approximation (GGA) is used as the exchange–correlation function and the double-zeta polarized basis set is employed in the calculations. The mesh cutoff energy is set to be 150 Ry and the *k*-point mesh is $1 \times 1 \times 100$ in the Monkhorst–Park scheme.[44] The vacuum spaces of the supercell are set to be more than 15 Å to eliminate interactions with adjacent images. All the atomic positions of the structure have been optimized until all the forces are smaller than 0.01 eV $Å^{-1}$. The edges of the ZC_3NNRs are terminated with hydrogen (H) atoms to remove the dangling bonds. For the pristine ZC_3NNRs, spin-polarized calculations with both ferromagnetic and antiferromagnetic initial guess converge to the nonmagnetic (NM) state,[45] so in this paper we focus on the NM state.

In NEGF theory, the current of the two-probe system is calculated based on the Landauer–Büttiker formula

$$I(V) = \frac{2e}{h}\int T(E,V)[f(E-\mu_L) - f(E-\mu_R)]\mathrm{d}E, \quad (1)$$

where $\mu_{L(R)}$ is the chemical potential of the left (right) electrode, $f(E-\mu_{L(R)})$ is the Fermi distribution of the left (right) electrode and $V = (\mu_L - \mu_R)/e$ represents the bias window. $T(E,V)$ is the transmission probability through the two-probe system which is obtained using Green's function

$$T(E,V) = \mathrm{Tr}[\Gamma_L(E,V)G^R(E,V)\Gamma_R(E,V)G^A(E,V)], \quad (2)$$

where $G^{R(A)}(E,V)$ is the retarded (advanced) Green's function of the scattering region and $\Gamma_{L(R)}$ is the coupling matrix to the left (right) electrode. Clearly, the current is determined by the area of the integral region in the bias window.

Results and discussions

Due to the heterogeneity with C and N elements, there are three possible edge morphologies by cutting a C_3N sheet into zigzag nanoribbons: (1) both edges are of all-carbon morphology, named *X*CC; (2) only one edge has N atoms, named *X*NC; (3) both edges have N atoms, called *X*NN, where *X* is the number of atoms along the nanowire in the direction of the width as shown in Fig. 1(a). We construct some C_3N-HJ devices composed of width-variable ZC_3NNRs. The left part is fixed with 9NC nanoribbon, but the

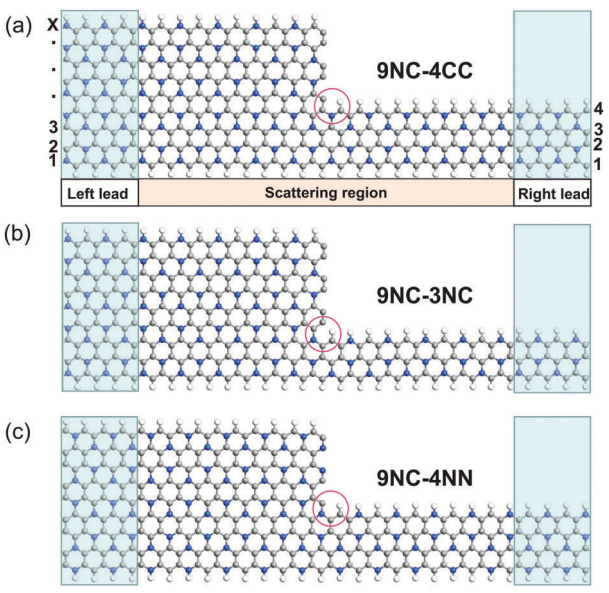

Fig. 1 Schematic illustrations of C_3N-HJ devices constructed of zigzag C_3N structures with different widths and different edges. (a) 9NC–4CC; (b) 9NC–3NC; (c) 9NC–4NN. Nitrogen, carbon and hydrogen atoms are shown by blue, gray and white balls, respectively.

right part has three edge morphologies with increasing width, including 4CC, 6CC, 8CC, 3NC, 5NC, 7NC, 4NN, 6NN and 8NN. Accordingly, the C_3N-HJ devices are classified into three types, labelled as 9NC–*X*CC, 9NC–*X*NC and 9NC–*X*NN respectively. For clarity, Fig. 1 shows schematic illustrations of 9NC–4CC, 9NC–3NC and 9NC–4NN devices. It is noteworthy that as the width of the right side increases, the step between the left and right sides reduces. It is significant to study the effects of the step and edge morphology on the electronic transport properties. In order to eliminate the influence of different interface structures as much as possible, for the same type of device, the bonding of atoms at the interface is consistent, marked with a circle in Fig. 1. Here, the atoms at the center interface are not passivated,[46,47] as a comparison, the H-passivated configurations will be discussed at the end. The total energies and edge energies of the C_3N-HJ devices have been calculated and are summarized in Table S1 (ESI†), showing good stability.[48,49]

Fig. 2 presents the current–voltage (*I*–*V*) characteristics of the ZC_3NNR-HJ devices. For 9NC–*X*CC devices, as shown in Fig. 2(a), these three *I*–*V* curves are approximately linear in the range of −0.3 V to 0.6 V and almost overlap each other, especially for 9NC–6CC and 9NC–8CC. As the forward bias increases, the current of 9NC–4CC continues to increase, but the currents of 9NC–6CC and 9NC–8CC begin to reduce, exhibiting NDR effects. As the reverse bias increases, the currents of 9NC–4CC and 9NC–6CC continue to increase, but at −0.4 V and −0.6 V respectively, the *I*–*V* curves start to become asymmetric with those at forward bias, indicating rectification behaviors. However, the current of 9NC–8CC behaves similarly at forward and reverse bias, both exhibiting NDR phenomena. It can be seen that when the step is larger, the rectification characteristics of the 9NC–*X*CC devices are more obvious, however when the step becomes smaller, the rectification gradually disappears and the NDR phenomenon is more prominent instead. In Fig. 2(b), the *I*–*V* characteristics of the 9NC–*X*NC devices are similar to those of the 9NC–*X*CC structures, except that the rectification effect of the 9NC–3NC and the NDR phenomena of the 9NC–5NC and 9NC–7NC are more obvious.

Surprisingly, for 9NC–*X*NN devices, their *I*–*V* characteristics are quite different from the first two. As shown in Fig. 2(c), all 9NC–*X*NN devices show forward-conducting and reverse-blocking rectifier diode characteristics. Interestingly, the current of the 9NC–6NN device is larger than that of the 9NC–8NN device which has a smaller step, so the current does not always increase as the step decreases. Structurally speaking, as can be seen from Fig. 1(c), 4NN is a non-mirror-symmetric structure, as is 8NN, but 6NN is a mirror-symmetric structure, so we suspect that the symmetry has a non-negligible influence on electron scattering as well.[50] In order to verify our idea, we add the 9NC–2NN calculation in Fig. 2(c). Sure enough, the current of 9NC–2NN is obviously larger than that of 9NC–4NN. Thus, for 9NC–*X*NN devices, the configuration of the right part is crucial for electron scattering. To more fully verify the impact of symmetry on the current magnitude, more models are needed for comparison by increasing the width of the left part, but in this study, we mainly focus on the rectification mechanism, so do not further expand here.

We select 9NC–5NC, 9NC–3NC and 9NC–6NN devices with significant NDR, rectification and diode effects respectively, and calculate their transmission spectra under different bias in Fig. 3. For the 9NC–5NC device, the transmission peak near the Fermi level becomes narrower as the bias increases. When the bias increases from 0.2 V to 0.6 V, although the transmission peak is narrowed a little, the integrated area is remarkably increased due to the enlarged bias window, thus the current becomes larger. However, as the bias continues to increase to 1.0 V, this transmission peak becomes significantly narrowed, resulting in a smaller integrated area, so that the current decreases and an NDR effect occurs. For the 9NC–3NC device, it is apparent that the transmission peak at 0.1 eV under a forward bias of 0.6 V is greatly suppressed under a reverse bias of −0.6 V, so the integration area is obviously reduced, and a significant rectification effect appears. As for the 9NC–6NN device, when a reverse bias of −0.6 V is applied, the transmission peak at −0.4 eV under a forward bias of 0.6 V is completely suppressed and there is no other transmission peak in the bias window, therefore the electrons in this system cannot be transmitted, inducing a forward-conducting and reverse-blocking rectifier diode effect. It is well-known that, the structure of the material determines the nature of the electronic transport, which we will discuss in detail in the next section.

Among the ZC_3NNRs with three types of edge morphology, 6CC, 5NC and 4NN are chosen as representatives to analyze their electronic structures. As shown in Fig. 4(a), comparing

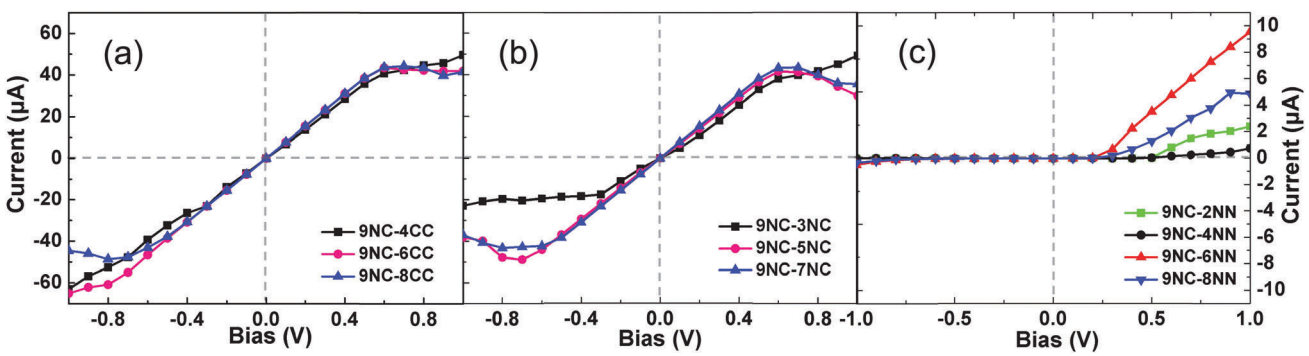

Fig. 2 The current–voltage curves of (a) 9NC–*X*CC; (b) 9NC–*X*NC; (c) 9NC–*X*NN ZC_3NNR-HJ devices in the bias range from −1.0 to 1.0 V.

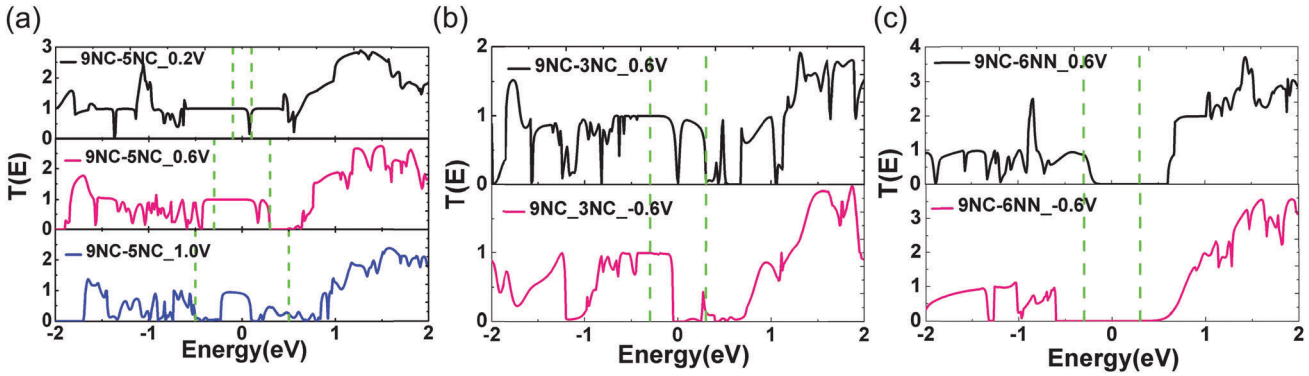

Fig. 3 The transmission spectra of (a) 9NC–5NC under bias of 0.2, 0.6 and 1.0 V; (b) 9NC–3NC under bias of 0.6 and −0.6 V; (c) The 9NC–6NN ZC_3NNR-HJ device under bias of 0.6 and −0.6 V. Zero energy is the Fermi level. The area between the green dotted lines is the bias window.

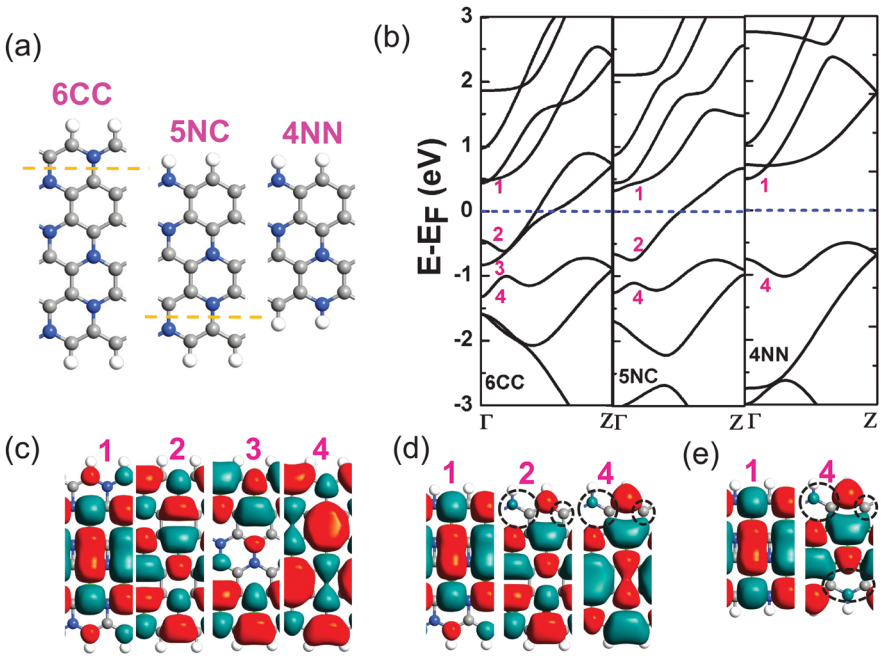

Fig. 4 (a) Schematic illustrations of 6CC, 5NC and 4NN ZC_3NNRs. The primitive cell is omitted, the same as below. Nitrogen, carbon and hydrogen atoms are shown by blue, gray and white balls, respectively. The cutting line is shown as orange dashed lines. (b) Band structures around the Fermi level of 6CC, 5NC and 4NN ZC_3NNRs. The blue dotted line is the Fermi level. Isosurface plots of the Γ-point wave functions of (c) n = 1, 2, 3, 4 subbands of 6CC ZC_3NNR; (d) n = 1, 2, 4 subbands of 5NC ZC_3NNR; (e) n = 1, 4 subbands of 4NN ZC_3NNR.

these three primitive cell structures, one can find that 5NC is equivalent to cutting the first row of a nanowire of 6CC, so an N atom appears at the upper edge. Similarly, 4NN is equivalent to cutting the last row of a nanowire of 5NC, and finally an N atom appears on both edges. Their band structures are calculated in Fig. 4(b). Both 6CC and 5NC have bands crossing the Fermi level, showing metallicity, while 4NN is an indirect band gap semiconductor. Interestingly, the number of bands crossing the Fermi level decreases gradually from 2 to 0. From a structural point of view, we can say that if one edge contains N atoms, the number of bands crossing the Fermi level will decrease by one (*i.e.*, n = 3 band disappears), and if both edges have N atoms, this number will continue to decrease by one (*i.e.*, n = 2 band disappears) and then becomes zero, so the ZC_3NNR changes from metal to semiconductor. It can be concluded that the edge morphology can effectively regulate the electronic properties of ZC_3NNRs. This deserves further study.

In Fig. 4(c–e) the wave functions of the bands near the Fermi level for the 6CC, 5NC and 4NN ZC_3NNRs are calculated respectively. The wave functions of the n = 1 bands of these three structures have the same distribution, all from the P_z orbitals of the C atoms of the pure carbon chain in the width direction of the nanoribbons, while the atoms in the *N*-containing chain do not contribute. As for the other two bands crossing the Fermi level, *i.e.*, n = 2 and n = 3, in the 6CC structure, the wave function of the n = 2 band derives from the P_z orbitals of all C and N atoms, but that of the n = 3 band is mainly from edge atoms, belonging to the edge state. When the nanowire at the

upper edge of 6CC is cut into 5NC, an N atom appears at the edge. Interestingly, almost no wave function is distributed over this N atom and its nearest C atoms (marked with a black dotted circle) in Fig. 4(d), but the other atoms are unaffected and still play the same role as 6CC, therefore the n = 2 band is little influenced and remains present in 5NC. However the n = 3 band is shown to be an edge state in 6CC, which is highly susceptible to edge atoms, so that this band does not exist near the Fermi level of 5CC. In addition, we also calculate the projected density of state (PDOS) of 5NC as depicted in Fig. S1 (ESI†), further verifying that the edge N atom and its nearest C atoms have little contribution to the DOS near the Fermi level. This similar phenomenon also occurs in B and N-doped ZGNRs[51] and C-doped zigzag BN nanoribbons (ZBNNRs),[52] it is found that the electrons preferentially flow from C to B, but the charge transfer from C to N is hampered due to large Coulomb repulsion on the N sites, resulting in the N atoms and connected C atoms contributing little to the DOS near the Fermi level.[51] So in our structures, it is the large Coulomb repulsion on edge N sites that hinders the electron transfer from the nearest C atoms, and further causes the state of the band crossing the Fermi level to be affected, thereby reducing its number. In 4NN, both edges have an N atom, therefore the n = 2 and n = 3 bands are more affected by the edge N atom and its nearest C atoms, resulting in neither of these bands being near the Fermi level. For the n = 4 band, the wave function is mainly from the P_z orbitals of the C atoms of the benzene ring in 6CC. In 5NC and 4NN, although the contribution of the edge N atom and its nearest C atoms is rare, the n = 4 band still exists due to the strong coupling between the C atoms on the benzene ring.

Furthermore, we also study the effect of width on the electronic structures of these three kinds of ZC_3NNR (as shown in Fig. S2, ESI†). For all *X*CC configurations, there are still two bands crossing the Fermi level, and as the width becomes larger, these two bands become more localized. For all *X*NC ZC_3NNRs, only one band crosses the Fermi level. For the *X*NN ZC_3NNRs, all structures are indirect band gap semiconductors, but the band gap reduces as the width increases. On the whole, the width has no essential effect on the electronic properties of ZC_3NNRs.

For clarity, the edge morphologies and properties of ZC_3NNRs and the electronic transport properties of the heterojunctions formed with 9NC are summarized in Table S2 (ESI†). We now look at the ZC_3NNR-HJ devices in Fig. 1, 9NC–*X*CC and 9NC–*X*NC devices are actually the combinations of two metallic structures, showing rectification and NDR effects, a similar phenomenon has also been found in graphene nanoribbons.[42] However, the 9NC–*X*NN device is a metal–semiconductor contact and presents very interesting diode behavior, in the following, we focus on the analysis of its inherent physical mechanism.

Selecting 9NC–4NN as the representative device to analyze, its left and right electrodes are 9NC and 4NN ZC_3NNRs respectively. If we apply a bias to the electrodes, a potential difference will appear between them, and their band structures will move relatively downward or upward. In Fig. 5(a), we apply a forward

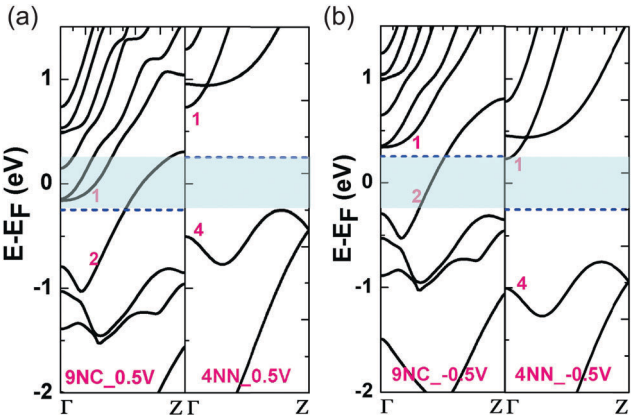

Fig. 5 Band structures around the Fermi level of the left and right electrodes of 9NC–4NN device (a) under forward bias of 0.5 V; (b) under reverse bias of −0.5 V. The band labels are the same as in Fig. 4. The blue dotted line is the Fermi level. The green rectangular area is the energy window.

bias of 0.5 V and an energy window (green shaded area) occurs due to the shift of the Fermi level. In this energy window, only the left electrode has several bands while the right electrode has a band gap between the valance band maximum (VBM) and the Fermi level, so electrons cannot jump from the right electrode to the left electrode, resulting in the prohibition of electron transmission. As the forward bias continues to increase, the n = 4 band of the right electrode will enter the energy window so that electrons can jump between the two electrodes and the device turns on, which explains why in Fig. 2(c), the positive cut-off bias of 9NC–4NN is 0.5 V. Fundamentally, the forward cut-off bias depends on the absolute value of the VBM of the right electrode, and the larger the value is, the larger the cut-off bias becomes. This value is about −0.5 eV for 2NN and 4NN, and about −0.3 eV for 6NN and 8NN, so the forward cut-off biases for their corresponding devices are 0.5 V and 0.3 V, respectively, as shown in Fig. 2(c).

Fig. 5(b) shows the band structures of the left and right electrodes after applying a reverse bias of −0.5 V. Like the mechanism under forward bias, electrons cannot jump in the energy window due to the band gap between the conduction band minimum (CBM) of right electrode and the Fermi level. However, the difference is that when the bias increases, the n = 1 band of the right electrode can enter into the energy window, so electron can jump, but the reverse current in Fig. 2(c) is still zero. We also test the wave functions of the n = 2 band of the left electrode and the n = 1 band of the right electrode as well as the higher band, and find there is no jumping limitation caused by symmetry, therefore these bands can be matched.[11,50] In this case, we guess that there is a potential barrier which prevents electrons from being transmitted. So we calculated the projected local density of states (PLDOS) in Fig. 6 to examine the interface barrier under different bias.

As shown in Fig. 6(a), the Fermi levels of the left and right parts of the 9NC–4NN device are aligned under thermal equilibrium state at zero bias. Furthermore, it is observed that the left part is metallic, while the right part is a semiconductor with

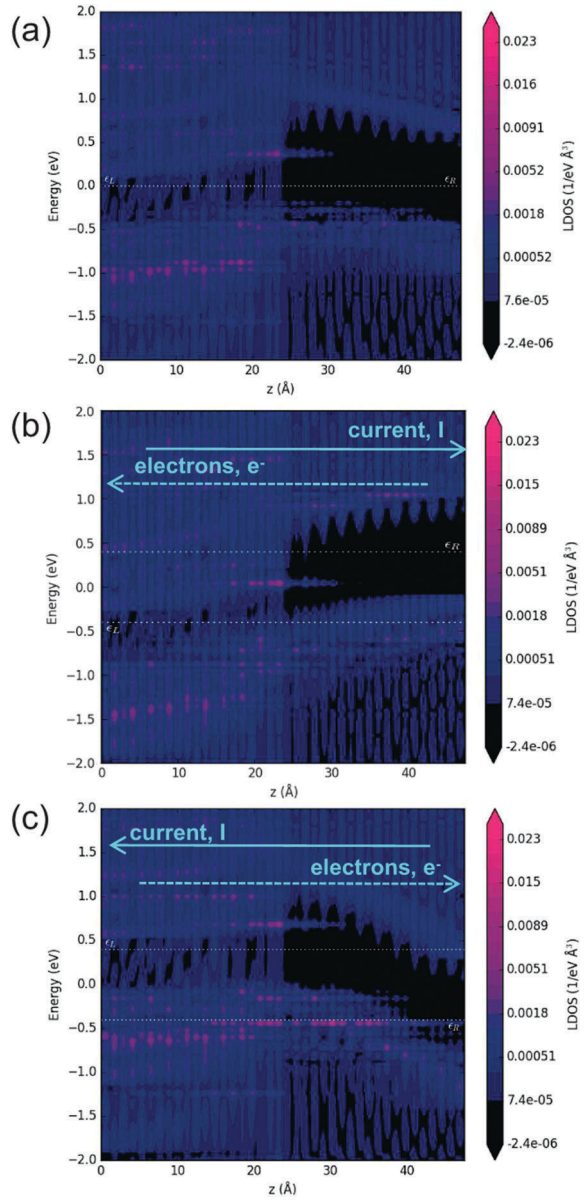

Fig. 6 The PLDOS plot of the 9NC–4NN device (a) at zero bias; (b) under forward bias of 0.8 V; (c) under reverse bias of −0.8 V. The abscissa indicates the Cartesian coordinate of the central region along the *Z* direction. The color bar indicates the DOS amplitude.

a band gap of about 1.0 eV which is consistent with the analysis of Fig. 4(b). In Fig. 6(b), When a forward bias of 0.8 V is applied, the chemical potential of the right electrode is energetically higher than that of the left electrode, so current flows from the left to the right electrode, and electrons flow from the right to the left electrode. Due to the rise of the Fermi level of the right side, the CBM and VBM near the Fermi level are bent upwards.[46] One can find that the electrons don't have to overcome any potential barrier at the interface during the flow, so the 9NC–4NN device has a large current under high forward bias.

In contrast, after a reverse bias of −0.8 V is applied, the chemical potential of the left electrode is energetically higher than that of the right electrode as shown in Fig. 6(c), so electrons flow from the left to the right electrode. However, although the left Fermi level moves upward under reverse bias, it is still lower in energy than the CBM of the right part at the interface, so a potential appears at the interface.[46,53] During the flow from the left to the right electrode, electrons must overcome this potential barrier, thus resulting in a very low current. Therefore the 9NC–4NN device is off at high reverse bias. Fundamentally, the potential barrier is still due to the semiconductor nature with the wide bandgap in the right part of metal–semiconductor HJ device.

Combined with practical applications, the device's interface atoms are H-passivated. The metal–metal contact 9NC–3NC and metal–semiconductor contact 9NC–4NN HJ structures are selected as representatives of passivation, as shown in Fig. 7(a), the H-passivated devices are named 9NC–3NC–H and 9NC–4NN–H, respectively. Table S1 (ESI†) shows that H-passivated devices have lower edge energies, and therefore have better stabilities. In Fig. 7(b), the *I–V* characteristics before and after passivation are compared. Obviously, for the 9NC–3NC device, the shape of the *I–V* curve after passivation does not change, and only slight changes in current under individual biases will not affect the overall electronic transport properties. This indicates that the change of interface barrier in the 9NC–3NC device after passivation is very small, so it can be said whether

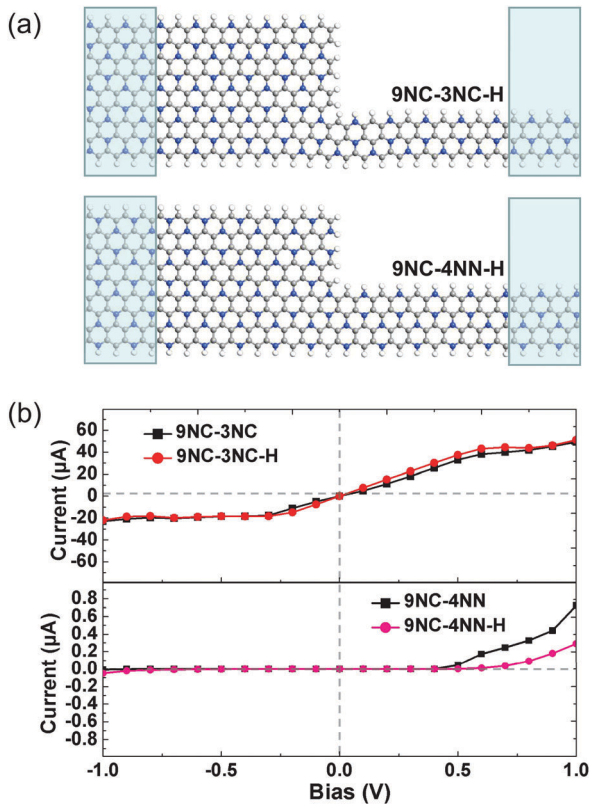

Fig. 7 (a) Schematic illustrations of 9NC–3NC–H and 9NC–4NN–H devices obtained by saturating the interface atoms of 9NC–3NC and 9NC–4NN devices with H atoms, respectively. (b) The current–voltage curves of 9NC–3NC–H and 9NC–4NN–H devices in the bias range from −1.0 to 1.0 V.

the interface is passivated with H atoms has little effect on the electronic transport properties of metal–metal contact devices such as 9NC–3NC. Compared with the 9NC–4NN device, the 9NC–4NN–H device also conducts at 0.5 V under forward bias, except that the on-state current is reduced, and also remains off within the bias range from −0.5 to 0.5 V. The cut-off range matches the band gap of the right electrode analyzed above. In addition, when the reverse bias exceeds −0.5 V and continues to increase, due to the decrease of the interface barrier after passivation, the current of the 9NC–4NN–H device is greater than that of the 9NC–4NN device, but the amplitude is small, so the overall electronic transport properties have changed little. Therefore, for the step-like ZC_3NNR-HJ devices, after passivation, our above mechanism analysis is still valid.

Defects (such as point defects) are generally unavoidable during sample preparation. Whether a point defect affects the electronic transport properties of the step-like ZC_3NNR-HJ devices is unknown. In Fig. S3 (ESI†), we further investigate the influences of point defects on rectification and NDR effects. It is found that, with the 9NC–3NC–H and 9NC–4NN–H devices as examples, a point defect near the step does not change the overall electronic transport properties, and the rectification and NDR effects are still very obvious, which provides a theoretical reference for the experiment.

Conclusions

In conclusion, we take advantage of the heterogeneity with C and N elements of a monolayer C_3N material, and construct several step-like HJ nanodevices composed of width-variable zigzag C_3N nanoribbons. It is found that the edge morphology of the ZC_3NNR causes disparate electronic structure and induces a variety of electronic transport properties. The ZC_3NNR is metallic as long as one edge is of all-carbon morphology, but becomes a semiconductor if both edges have N atoms. NDR and rectification effects appear in the metal–metal contact 9NC–*X*CC and 9NC–*X*NC HJ devices, and the larger the interface step, the more significant the rectification phenomenon, and the smaller the interface step, the more obvious the NDR effect. Interestingly, a forward-conducting and reverse-blocking rectifier diode behavior occurs in metal–semiconductor contact 9NC–*X*NN HJ devices. This is mainly caused by the band structure of the right electrode and the interface potential barrier. Due to the large band gap of the right electrode, the device cuts off at low bias, and as the reverse bias continues to increase, the device remains off due to the presence of an interface barrier. When the interface of the device is passivated with H atoms, the electronic transport properties do not change much, and the mechanism is equally applicable. Furthermore, a point defect near the step will not affect the overall electronic transport properties, and the rectification and NDR effects are still very obvious. It can be seen that the simple tailoring method and abundant electronic transport properties of C_3N materials facilitates the application in the field of nanoelectronic devices.

Conflicts of interest

There are no conflicts to declare.

Acknowledgements

This work is supported by the National Natural Science Foundation of China (NSFC11504178, NSFC11374162, NSFC11247033 and NSFC51651202), the Natural Science Foundation of Jiangsu Province (BK20150825 and TJ215009), the Scientific Research Foundation of Nanjing University of Posts and Telecommunications (NY214010 and NY217013) and the Fundamental Research Funds for the Central Universities (NS2014073).

References

1 L. P. Biró, P. Nemes-Incze and P. Lambin, *Nanoscale*, 2012, **4**, 1824–1839.
2 Q. Yan, B. Huang, J. Yu, F. Zheng, J. Zang, J. Wu, B. Lin Gu, F. Liu and W. Duan, *Nano Lett.*, 2007, **7**, 1469.
3 J. He, K. Q. Chen, Z. Q. Fan, L. M. Tang and W. P. Hu, *Appl. Phys. Lett.*, 2010, **97**, 239.
4 T. Chen, Y. Xue, A. K. Roy and L. Dai, *ACS Nano*, 2014, **8**, 1039–1046.
5 S. Yang, W. Li, C. Ye, G. Wang, H. Tian, C. Zhu, P. He, G. Ding, X. Xie and Y. Liu, *Adv. Mater.*, 2017, **29**, 1605625.
6 J. Mahmood, E. K. Lee, M. Jung, D. Shin, H. J. Choi, J. M. Seo, S. M. Jung, D. Kim, F. Li and M. S. Lah, *Proc. Natl. Acad. Sci. U. S. A.*, 2016, **113**, 7414.
7 Q. Hu, Q. Wu, H. Wang, J. He and G. Zhang, *Phys. Status Solidi*, 2012, **249**, 784–788.
8 Y. Feng, X. Yao, M. Wang, Z. Hu, X. Luo, H. T. Wang and L. Zhang, *J. Chem. Phys.*, 2013, **138**, 164706.
9 M. Eslami, M. Moradi and R. Moradi, *Vacuum*, 2016, **133**, 7–12.
10 H. Wang, H. Wu and J. Yang, 2017, **1703**, 08754, arXiv preprint arXiv:1703.08754.
11 Z. F. Wang, Q. Li, Q. W. Shi, X. Wang, J. Yang, J. G. Hou and J. Chen, *Appl. Phys. Lett.*, 2008, **92**, 197.
12 H. Ren, Q. X. Li, Y. Luo and J. Yang, *Appl. Phys. Lett.*, 2009, **94**, 666.
13 X. F. Li, K. Y. Lian, Q. Qiu and Y. Luo, *Nanoscale*, 2015, **7**, 4156–4162.
14 Y. An, K. Wang, G. Jia, T. Wang, Z. Jiao, Z. Fu, X. Chu, G. Xu and C. Yang, *RSC Adv.*, 2014, **4**, 46934–46939.
15 J. Zeng, K. Q. Chen, J. He, X. J. Zhang and C. Q. Sun, *J. Phys. Chem. C*, 2011, **115**, 25072–25076.
16 A. Kargar and C. Lee, *Nanotechnology, 2009. IEEE-NANO 2009. 9th IEEE Conference on. IEEE*, 2009, vol. 8, pp. 243–245.
17 J. Peng, Y. H. Zhou and K. Q. Chen, *Org. Electron.*, 2015, **27**, 137–142.
18 T. Ozaki, K. Nishio, H. Weng and H. Kino, *Phys. Rev. B: Condens. Matter Mater. Phys.*, 2010, **81**, 1–11.
19 J. Zheng, X. Yan, L. Yu, H. Li, R. Qin, G. Luo, Z. Gao, D. Yu and J. Lu, *J. Phys. Chem. C*, 2011, **115**, 8547–8554.

20 C. Cao, Y. Wang, H. P. Cheng and J. Z. Jiang, *Appl. Phys. Lett.*, 2011, **99**, 666.
21 G. P. Tang, J. C. Zhou, Z. H. Zhang, X. Q. Deng and Z. Q. Fan, *Carbon*, 2013, **60**, 94–101.
22 G. Liu, X. Zhuang, Y. Chen, B. Zhang, J. Zhu, C. X. Zhu, K. G. Neoh and E. T. Kang, *Appl. Phys. Lett.*, 2009, **95**, 327.
23 Y. Chen, B. Zhang, G. Liu, X. Zhuang and E. T. Kang, *Chem. Soc. Rev.*, 2012, **41**, 4688.
24 S. H. Lee, M. Choi, T. T. Kim, S. Lee, M. Liu, X. Yin, K. C. Hong, S. S. Lee, C. G. Choi and S. Y. Choi, *Nat. Mater.*, 2012, **11**, 936–941.
25 X. Wang, Y. Ouyang, X. Li, H. Wang, J. Guo and H. Dai, *Phys. Rev. Lett.*, 2008, **100**, 206803.
26 P. Zhao, R. M. Feenstra, G. Gu and D. Jena, *IEEE Trans. Electron Devices*, 2013, **60**, 951–957.
27 K. Nagashio, T. Nishimura, K. Kita and A. Toriumi, *Jpn. J. Appl. Phys.*, 2010, **49**, 311–333.
28 R. M. Metzger, *Chem. Rev.*, 2003, **103**, 3803–3834.
29 J. Hu, X. Ruan and Y. P. Chen, *Nano Lett.*, 2009, **9**, 2730.
30 L. Xie, S. Z. Chen, W. X. Zhou and K. Q. Chen, *Org. Electron.*, 2017, **46**, 150–157.
31 X. F. Li, L. L. Wang, K. Q. Chen and Y. Luo, *J. Phys.: Condens. Matter*, 2012, **24**, 095801.
32 A. S. Martin, J. R. Sambles and G. J. Ashwell, *Phys. Rev. Lett.*, 1993, **70**, 218.
33 N. J. Tao, *Nat. Nanotechnol.*, 2006, **1**, 173–181.
34 R. M. Metzger, *Adv. Funct. Mater.*, 1998, **8**, 10455–10466.
35 Z. Q. Fan, W. Y. Sun, X. W. Jiang, J. W. Luo and S. S. Li, *Org. Electron.*, 2017, **44**, 20–24.
36 X.-F. Li, L.-L. Wang, K.-Q. Chen and Y. Luo, *J. Phys. Chem. C*, 2011, **115**, 12616–12624.
37 C. Cao, L.-N. Chen, M.-Q. Long and H. Xu, *Phys. Lett. A*, 2013, **377**, 1905–1910.
38 A. Cadore, E. Mania, E. De Morais, K. Watanabe, T. Taniguchi, R. Lacerda and L. Campos, *Appl. Phys. Lett.*, 2016, **109**, 033109.
39 L. Peng, K. Yao, S. Zhu, Y. Ni, F. Zu, S. Wang, B. Guo and Y. Tian, *J. Appl. Phys.*, 2014, **115**, 223705.
40 A. F. Young and P. Kim, *Nat. Phys.*, 2009, **5**, 222.
41 C. Ma, L. Liang, Z. Xiao, A. A. Puretzky, K. Hong, W. Lu, V. Meunier, J. Bernholc and A.-P. Li, *Nano Lett.*, 2017, **17**, 6241–6247.
42 Y. An, K. Wang, Z. Yang, Z. Liu, G. Jia, Z. Jiao, T. Wang and G. Xu, *Org. Electron.*, 2015, **17**, 262–269.
43 M. Brandbyge, J.-L. Mozos, P. Ordejón, J. Taylor and K. Stokbro, *Phys. Rev. B: Condens. Matter Mater. Phys.*, 2002, **65**, 165401.
44 H. Monkhorst and J. Pack, *Phys. Rev. B: Solid State*, 1976, **13**, 5188.
45 C. Cao, M. Wu, J. Jiang and H. Cheng, *Phys. Rev. B: Condens. Matter Mater. Phys.*, 2010, **81**, 205424.
46 W. Zhang, C. Basaran and T. Ragab, *Carbon*, 2017, **124**, 422–428.
47 Y.-D. Guo, H.-F. Liu, H.-L. Zeng, X.-H. Yan and X.-C. Song, *Phys. Chem. Chem. Phys.*, 2018, **20**, 9241–9247.
48 P. Koskinen, S. Malola and H. Häkkinen, *Phys. Rev. Lett.*, 2008, **101**, 115502.
49 B. Huang, M. Liu, N. Su, J. Wu, W. Duan, B. L. Gu and F. Liu, *Phys. Rev. Lett.*, 2009, **102**, 166404.
50 Z. Li, H. Qian, J. Wu, B. L. Gu and W. Duan, *Phys. Rev. Lett.*, 2008, **100**, 206802.
51 S. Dutta, A. K. Manna and S. K. Pati, *Phys. Rev. Lett.*, 2009, **102**, 096601.
52 S. Tang and Z. Cao, *Phys. Chem. Chem. Phys.*, 2010, **12**, 2313–2320.
53 Z. Yang, J. Pan, Q. Liu, N. Wu, M. Hu and F. Ouyang, *Phys. Chem. Chem. Phys.*, 2017, **19**, 1303–1310.

